

# Chirp-dependent dual light emission in $\text{Na}_{0.95}\text{Er}_{0.05}\text{Nb}_{0.9}\text{Ti}_{0.1}\text{O}_3$ perovskite

Óscar Pérez-Benito<sup>a</sup>, Miguel Ángel Antón<sup>b</sup>, Esteban Urones-Garrote<sup>c</sup>, Susana García-Martín<sup>d</sup>, Ester García-González<sup>d,\*</sup> and Rosa Weigand<sup>a,\*\*</sup>

<sup>a</sup>Department of Optics, Faculty of Physics, Universidad Complutense de Madrid, Avenida Complutense s/n, Madrid, 28040, Spain

<sup>b</sup>Department of Optics, Faculty of Optics and Optometry, Universidad Complutense de Madrid, Calle Arcos de Jalón, 118, Madrid, 28037, Spain

<sup>c</sup>ICTS Centro Nacional de Microscopía Electrónica, Faculty of Chemistry, Universidad Complutense de Madrid, Avenida Complutense s/n, Madrid, 28040, Spain

<sup>d</sup>Department of Inorganic Chemistry, Faculty of Chemistry, Universidad Complutense de Madrid, Avenida Complutense s/n, Madrid, 28040, Spain

## ARTICLE INFO

### Keywords:

Perovskites

Polar sodium niobate

Up-conversion fluorescence

Second-Harmonic Generation

Coherent Light Control

## Abstract

Polar  $\text{Na}_{0.95}\text{Er}_{0.05}\text{Nb}_{0.9}\text{Ti}_{0.1}\text{O}_3$  perovskite has been synthesized as a nanostructured material by microwave assisted hydrothermal method. The characterization indicates that erbium is a constituent of the crystal structure and is preferentially located in sodium positions. The compound combines the nonlinear optical properties of the host ( $\text{NaNb}_{0.9}\text{Ti}_{0.1}\text{O}_{2.95}$ ) and the fluorescent properties of the  $\text{Er}^{3+}$ -dopant. Under excitation by a single femtosecond ( $< 10$  fs) laser in the near-infrared region, simultaneous dual emission signals of second harmonic generation (SHG) and up-converting fluorescence (UCF) are observed and the nonlinear dependencies of the SHG and UCF intensities on the excitation intensity are measured. In addition, both emissions are shown to be sensitive to the chirp of the exciting pulses, and for UCF, it can be explained by means of a simple theoretical model based on the density matrix equations. These nano-structured particles with chirp-dependent dual behavior can be very advantageous when used in biological systems, since they can provide complementary information in different spectral ranges and tissues and are susceptible of coherent control, which can be both useful in optical microscopy and bioimaging.

## 1. Introduction

Development of materials with excellent fluorescent and nonlinear optical properties has been a highly active area of research for a wide variety of promising applications, including optoelectronic devices, microfabrication, bioimaging, and photodynamic therapy. [1–5].

A key challenge in fluorescence microscopy is to find suitable fluorescent markers or probes that, when attached to specific proteins or compounds, allow for an easy observation during a sufficient amount of time [6]. Commonly used fluorescent markers in the visible part of the spectrum are organic dyes, which are often problematic as they undergo degrading photo-induced processes such as blinking and bleaching that limit the stability of the experiment and the amount of detectable photons. Additionally, some biological samples present self-fluorescence in the visible range of the spectrum that may overlap with the emission of the markers, which is an important source of noise in the measurement [7, 8]. To circumvent some of these limitations, in the last years new approaches have been introduced using non-organic systems such as metallic nanoparticles (NPs), semiconductor quantum dots (QDs), up-converting fluorophores (UCF) and second harmonic nanoparticles [9]. Among them, rare earth doped inorganic nanocrystals have numerous applications in modern biosensing, ranging from

*in vitro* and *in vivo* fluorescence imaging to intracellular thermal sensing. In this sense, doping with lanthanide ( $\text{Ln}^{3+}$ ) elements or co-doping with ytterbium ( $\text{Yb}^{3+}$ ) and erbium ( $\text{Er}^{3+}$ ) ions, have recently emerged as a serious alternative to both QDs and gold nanorods (GNRs) for biomedical imaging [9, 10].


Due to their particular electronic configurations, rare-earth ions usually present a rich energy level diagram.

In comparison to QDs and GNRs, the two-photon excited fluorescence (upconversion) spectrum, obtained for example from typical  $\text{NaYF}_4:\text{Er}^{3+}$  NPs under NIR excitation, is characterized by well-defined structured emission bands in the red, green and blue spectral ranges [11], which are independent of particle size, shape and environment. Thus, up-converting nanoparticles (UCNPs) have been widely employed in bioimaging, diffusion optical tomography, bio-sensing and photodynamic therapy (PDT) [9, 11].

Other than UC fluorescent nanoparticles, compounds emitting via second harmonic generation (SHG) are the subject of an increasing number of studies. Emitter compounds such as  $\text{Fe}(\text{IO}_3)_3$ ,  $\text{ZnO}$ ,  $\text{KNbO}_3$ ,  $\text{LiNbO}_3$ ,  $\text{BaTiO}_3$  or KTP (Potassium Titanyl Phosphate) have been reported and rather complete overviews of SHG in nanoparticles are available in the literature [5, 12]. Since SHG involves transitions only through virtual energy levels, it possesses a series of attractive properties, such as complete absence of bleaching and blinking and coherent optical response. Moreover, the infinitely photo-stable signal guaranteed by harmonic nanoparticles makes them ideal probes for long-term cell

\*Corresponding author

\*\*Corresponding author

 esterg@quim.ucm.es (E. García-González); weigand@fis.ucm.es

(R. Weigand)

ORCID(s):

tracking. In addition, the absence of phase matching requirements for SHG allows for a large tunability of the excitation wavelength and provides the possibility to frequency-double the full spectrum of broadband laser sources. These harmonic particles can be coherently excited with IR wavelengths, which prevents tissues degradation and improves spatial resolution due to the quadratic dependence of the excitation process with intensity. Furthermore, while the excitation lifetime of common fluorescent probes is on the order of nanoseconds, SHG emission is almost instantaneous to the excitation, allowing for ultrafast modulation and coherent control of the signal. As a result, SHG probes act as subwavelength coherent photon sources. This is a great advantage, since it allows to detect the complex SHG signal by interferometric approaches offering opportunities for new imaging techniques, such as scan-free 3D imaging.

Since UCF and SHG processes involve different contrast mechanisms, a multimodal contrast agent would be highly interesting in applications such as bioimaging, to provide complementary information regarding tissue structure and its function. In this context, the core-shell KTP-Eu system, obtained by synthesizing  $\text{KTP@LaPO}_4\text{:Eu}$  nanoparticles shows both SHG and UCF emission [13] but a complex optical system constituted by two lasers must be used in order to produce the dual process. Simultaneous observation of SHG and UCF signals has been recently reported by exciting erbium doped  $\alpha\text{-La}_{0.85}\text{Er}_{0.15}(\text{IO}_3)_3$  nanocrystals in suspension with a single tunable femtosecond laser [14]. UCF has also been observed in a rare-earth doped perovskite ( $\text{Eu:BaTiO}_3$ ), but SHG properties were not reported [15].

Taking advantage of the polar properties of  $\text{NaNb}_{0.9}\text{Ti}_{0.1}\text{O}_{2.95}$ , we have prepared nano-structured  $\text{Na}_{0.95}\text{Er}_{0.05}\text{Nb}_{0.9}\text{Ti}_{0.1}\text{O}_3$ , with  $\text{Er}^{3+}$  ions as luminescent emitters. We demonstrate in this work that  $\text{Na}_{0.95}\text{Er}_{0.05}\text{Nb}_{0.9}\text{Ti}_{0.1}\text{O}_3$  perovskite can simultaneously generate a strong SHG signal, along with UCF at room temperature when excited by a single broadband house-made Titanium:Sapphire laser oscillator with just a few femtoseconds pulse duration.

To manipulate ultrafast light-matter interactions at the nanoscale by using precisely tailored laser fields, is a highly interesting concept that is often referred to as coherent control. Particularly, coherent control of various nonlinear optical processes in atomic and molecular systems, such as two-photon or multiphoton absorption [16–18], and high order harmonic generation [19, 20], have been addressed. If the SHG and UCF emissions could be artificially enhanced, suppressed, or tuned, its applications could be greatly extended in studies requiring higher energies, for example, in real-time applications and faster super-resolution bioimaging [9]. Nowadays, various femtosecond pulse shaping techniques have been proposed to control the up conversion fluorescence in two-photon fluorescence in  $\text{Er}^{3+}$  ions by a  $\pi$ -phase modulation [21]. In this context, we have analyzed the dependence of the SHG and UCF signals on the chirp of the pulses as an indication that the synthesized particles are suitable for a coherent control of the obtained emissions.

## 2. Experimental

### 2.1. Synthesis

The microwave assisted hydrothermal reactions were performed in a commercial microwave-hydrothermal system Milestone Ethos One. Based on the newly reported polar Ti-substituted sodium niobate  $\text{NaTi}_x\text{Nb}_{1-x}\text{O}_{3-0.5x}$  and its stability upon annealing [22], we have synthesized  $\text{NaNb}_{0.9}\text{Ti}_{0.1}\text{O}_{2.95}$  (NNT) and  $\text{Na}_{0.95}\text{Er}_{0.05}\text{Nb}_{0.9}\text{Ti}_{0.1}\text{O}_3$  (Er-NNT). For the synthesis of NNT,  $\text{Nb}_2\text{O}_5$  (Sigma-Aldrich, 99,99%) and HCl stabilized  $\text{TiCl}_4$  (Sigma-Aldrich, 0.09 M) were used as starting reagents.  $\text{Nb}_2\text{O}_5$  (2.84 mmol) was dispersed in 20 mL of a 12 M NaOH solution and after stirring during 10 min, 7 mL of  $\text{TiCl}_4$  (0.63 mmol) were added. For Er-NNT, the same amounts of  $\text{Nb}_2\text{O}_5$  and  $\text{TiCl}_4$  were used and dispersed in 20 mL of a 11.4 M NaOH solution to which 0.302 mmol of  $\text{Er}(\text{NO}_3)_3 \cdot 5\text{H}_2\text{O}$  (Sigma-Aldrich, 99,9%) were added. The final solution was then placed into a double-walled vessel consisting of an inner polytetrafluoroethylene (PTFE) container and an outer case made of another polymer. Both polymers are transparent to microwave irradiation. The system also includes a temperature sensor and pressure control in the vessel. The microwave system was programmed with a heating rate of  $17.5^\circ\text{C}/\text{min}$  to the treatment temperature of  $200^\circ\text{C}$  for 1 hour. The power was limited to 600 W and the autogenous pressures achieved during the experiment were 11 and 12 bar for NNT and Er-NNT, respectively. Stirring was maintained during the experiments. The obtained products were centrifuged (8000 rpm, 5 min), rinsed with distilled water twice and dried at  $80^\circ\text{C}$  for 12 hours. Annealing treatments were performed in air at  $600^\circ\text{C}$  for 6 hours with heating and cooling rates of  $2^\circ\text{C}/\text{min}$ . The resulting color of powdered solids obtained were white and light pink, for NNT and Er-NNT, respectively.

### 2.2. Methods

Room temperature powder X-ray diffraction (XRD) patterns were obtained in a Panalytical X'PERT PRO MPD diffractometer with a  $\text{Ge}(111)$  primary beam monochromator prealigned for  $\text{Cu K}\alpha$  radiation ( $\lambda = 1.5418 \text{ \AA}$ ) with an X'Celerator fast detector. Data were collected between  $5$  and  $90^\circ 2\theta$  with an effective step time of 15 s and a step size of  $0.017^\circ 2\theta$ . Samples for transmission electron microscopy (TEM) were ultrasonically dispersed in n-butanol and transferred to carbon coated copper grids. Selected area electron diffraction (SAED) and high-resolution transmission electron microscopy (HRTEM) were performed on a JEOL JEM300F electron microscope by working at 300 kV (point resolution of 0.17 nm). Crystal-by-crystal chemical microanalysis was performed by energy-dispersive X-ray spectroscopy (XEDS) in the same microscope equipped with an ISIS 300 X-ray microanalysis system (Oxford Instruments) with a detector model LINK "Pentafet" (resolution 135 eV). Electron energy-loss spectroscopy (EELS) experiments were performed on a ARM200cF microscope, fitted with a condenser lens aberration corrector (point resolution in STEM mode of 0.08 nm) and equipped with a GIF

Quantum-ER Spectrometer. EELS mapping was performed with a collection semi-angle  $\beta \sim 30$  mrad, 1 eV per channel dispersion and a collection time for each spectrum of 0.1 seconds. Er-M<sub>4,5</sub>, Na-K and Nb-L<sub>2,3</sub> edge signals were chosen for mapping.

### 2.3. Optical set-up

For the characterization of the optical properties, colloidal suspensions of NNT and Er-NNT particles in n-butanol were sonicated for 15 minutes. Several 2  $\mu\text{l}$  drops from the supernatant were added and uniformly distributed into a standard borosilicate 150  $\mu\text{m}$ -thick microscope coverslip (see inset in Figure 1) until the desired linear optical transmittance  $T$  was reached ( $T \sim 50\%$  using the Titanium:Sapphire laser described below, operating in CW).

Figure 1 shows the setup used for exciting the SHG and the UCF signals with ultrashort laser pulses, as well as the detection system. The aim is not only to produce SHG and UCF, but also to detect if the system is sensitive to the chirp of the pulses, i.e. to the distribution of wavelengths in time within the pulse, in order to identify the existence of coherent processes. For that purpose, pulses from a house-made horizontally-polarized broadband Ti:Sa oscillator were used [23].

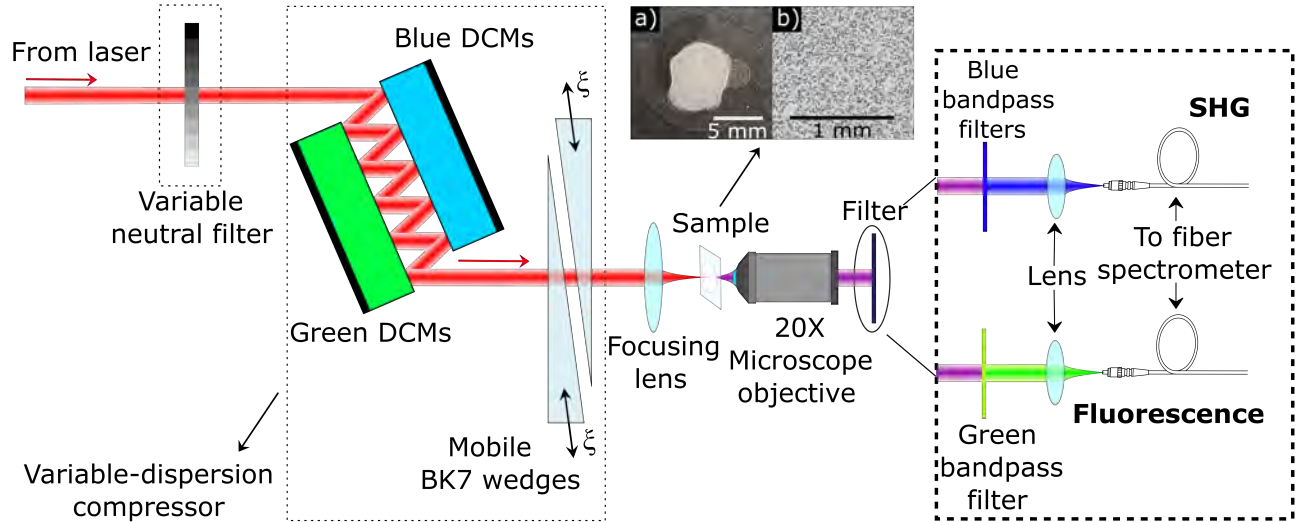


**Figure 1:** Experimental set-up for the generation and detection of SHG and UCF signals with different chirped pulses. Neutral filters used only for the intensity response measurements. Inset: a) Camera image, b) Optical microscope image of a typical Er-NNT sample.

Briefly, the system produces pulses about 10 fs of duration at 80 MHz repetition rate, and by changing the position of several intracavity components of the laser, the distribution of wavelengths in time within the pulse spectrum of the laser can be changed. Figure 2 shows two different spectra both peaked at 766 nm but with or without spectral content around 980 nm. Hence, the laser pulses always have spectral content at 796 nm and only in case a) at 980 nm, while  $\text{Er}^{3+}$  ions can be excited at both wavelengths [24].

Once the spectrum is chosen, the chirp of the pulses can be changed using a variable-dispersion compressor (Figure

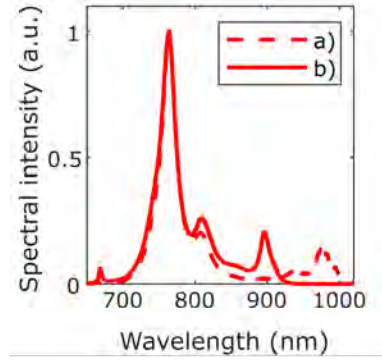


**Figure 2:** Spectrum of the Ti:Sa laser oscillator for two different intracavity dispersion values, a) with an emission band around 980 nm and b) without it.

1). That way we can produce negatively chirped pulses, pulses at the maximum-compression point or positively chirped pulses. The average power at the exit of the wedges was between 40-45 mW.

The laser pulses were then focused using a 1 cm focal-length lens on the sample and the generated signals were collected using a 20 $\times$  microscope objective. To detect the SH-signal, color filters Schott BG37 and BG12 were used, while for detecting the UCF signal a bandpass filter at 550 nm (FESH0550 from Thorlabs) was used. Once filtered, the corresponding signal was focused onto a solarized optical fiber with a nucleus diameter of 400  $\mu\text{m}$  coupled to a spectrometer (Ocean Optics HR4000). This system has been previously described [25] using  $\text{BaTiO}_3$  nanoparticles to measure the sub-7 fs pulses from the oscillator. The



accumulation time needed to have reasonable signals (2000–10000 counts) varied from 200 to 1000 ms in NNT and Er-NNT samples. The generated signals were not polarized, as expected for a system of randomly oriented crystallites.

### 3. Results and discussion

#### 3.1. Structural and microstructural characterization

$\text{NaNbO}_3$  perovskite exhibits an unusually large number of phase transitions upon variation of temperature, owing to oxygen octahedra tilting and off-centered displacement of Nb ions, thus giving rise to a structurally very complex perovskite material. The room temperature stable phase commonly referred as the P phase (space group  $Pbma$ ) coexists at ambient conditions with the metastable Q phase (space group  $P2_1ma$ ). This coexistence prevents the appearance of the polar properties. Doping, either in Na, in Nb or in O sublattices, is a common approach to stabilize the polar polymorph at room temperature [26, 27]. In this sense, as mentioned, our doping strategy involves niobium sublattice to obtain polar NNT.

The room temperature antiferroelectric polymorph of  $\text{NaNbO}_3$  (P) exhibits an uncommon octahedral tilting leading to a  $\sqrt{2}a_c \times 4a_c \times \sqrt{2}a_c$  supercell (where  $a_c$  represents the unit cell parameter of the cubic perovskite) [28]. The resulting phase is non-polar by symmetry, the dipole moments from antiparallel  $\text{Nb}^{5+}$  displacements being cancelled within the unit cell. In the coexisting polar Q phase,  $\text{Nb}^{5+}$  displacements occur in the same direction, thus leading to a  $\sqrt{2}a_c \times 2a_c \times \sqrt{2}a_c$  supercell [29].

Powder X-ray diffraction patterns obtained for NNT as well as for Er-NNT, were compatible with the non-centrosymmetric Q phase (Figure A1). However, the close structural relationship between the P and the Q phase [30], together with the relatively broad diffraction maxima obtained, could hinder to distinguish the right symmetry of both materials.

In this sense, and to unambiguously determine the crystal symmetry of the materials, the microstructural study by means of transmission electron microscopy was performed. The microstructure and crystal morphology of both, the doped and the undoped material, are analogous. Synthesized materials are made up of platelet like crystallites (average size  $\sim 100$  nm) that in turn are formed by nanometric crystalline domains. This is probably a consequence of the synthetic method used.

Figure 3 displays two micrographs corresponding to a crystal of a) NNT and b) Er-NNT, oriented in the  $[010]_C$  zone axis. This structure projection does not allow to distinguish between the two phases and d spacing of  $\sim 0.4$  nm can be measured in two perpendicular directions, which can be assigned to  $a_c$ . In addition, d spacing of  $\sim 0.58$  nm is observed, which correspond to  $a/c$  unit cell parameters of the P and Q phases. In the included Fourier Transforms (FTs), the width of the diffraction maxima is highlighted,

which is in accordance with the small size of the crystalline domains that make up each crystallite.

As mentioned, the unit cells of the P and Q phases are quadrupled and doubled, respectively, in the  $[010]$  direction of the prototype cubic perovskite unit cell. Then, superlattice diffraction maxima at  $1/4\{010\}$  for the P phase, and  $1/2\{010\}$  for the Q phase, must be observed in the corresponding electron diffraction patterns or the FTs. Figure 4 shows the high-resolution electron micrograph of a crystal of a) NNT and b) Er-NNT in the  $[001]_C$  zone axis. Insets on each micrograph show the corresponding FTs; doubling of the  $[010]$  direction is observed by the presence of  $1/2\{010\}$  superlattice diffraction maxima, thus confirming the symmetry of the Q phase in both oxides.

It is essential to confirm the polar nature of the synthesized materials, but it is also important to determine the dopant content and location in the host crystal structure provided that we look for combining the SHG and UCF capabilities. Photoluminescence properties can be modified significantly depending on dopant concentration as well as on its crystallographic location in the host structure. The crystal-by-crystal XEDS microanalysis performed, indicates that erbium in the Er-NNT compound is a bulk constituent of the crystals, and is not segregated as  $\text{Er}_2\text{O}_3$  or in the form of a secondary phase. The atomic ratio of the metals, determined by XEDS analysis, indicates good agreement between analytical and nominal composition in all the crystals of the sample. The atomic percentage of erbium varies in the range  $\sim 3 - 5$  atomic % from crystal to crystal.

In order to elucidate the location of erbium in the crystal structure, the atomic distribution of Er-NNT was investigated by HAADF STEM imaging. Figure 5 a) shows the HAADF-STEM micrograph of a crystal of Er-NNT in the  $[100]_Q$  ( $[110]_C$ ) projection. Under these imaging conditions, contrast scales with the square of the atomic number  $Z$ , and light elements such as oxygen or sodium can hardly be detected. Therefore, the lines of bright spots observed are interpreted as corresponding to columns of Nb/Ti atoms in alternate (001) planes, columns of sodium and oxygen atoms making a negligible contribution to the image contrast. Figure 5 b) shows the variation of the intensity of the Nb- $L_{2,3}$ , Na-K and Er- $M_{4,5}$  edge signals obtained from an EELS line-scan along the  $[001]$  direction on the columns of atoms indicated by the yellow line in the image. Although the Er- $M_{4,5}$  edge signal is very noisy since erbium is in low concentration in the crystals, it is clearly observed that maxima in sodium and erbium profiles can be assigned to the same structural positions, which in addition correspond to the minima of niobium profile. These results confirm that erbium substitute for sodium in the A sites of perovskite. Furthermore, small regions of 1–3 nm with bright contrast in (Na/Er)-O planes are visible, which must correspond to erbium enriched zones.

The TEM results thus confirm the formation of the non-centrosymmetric phase, the Q-phase, and therefore, we can expect SHG emission. In addition to the SHG, Er-doping can generate fluorescence emission. In this sense,

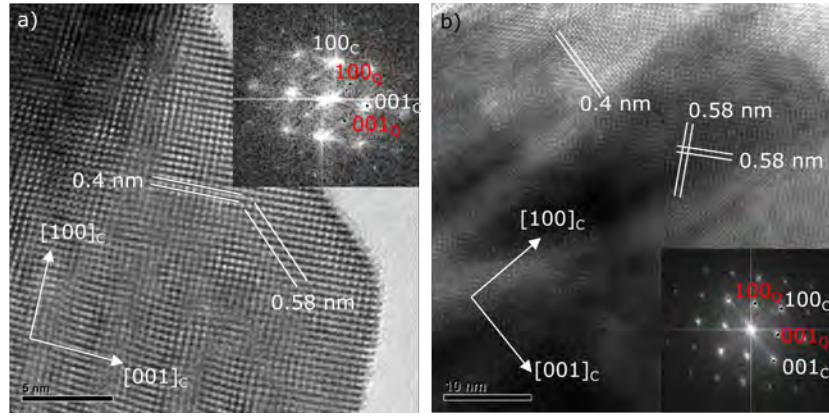


**Figure 3:** High resolution electron micrograph of a crystal of a) NNT and b) Er-NNT in the  $[010]_C$  zone axis. Insets show the corresponding Fast Fourier Transform, where Miller index in white and red correspond to the basic perovskite cell and to the Q phase, respectively.

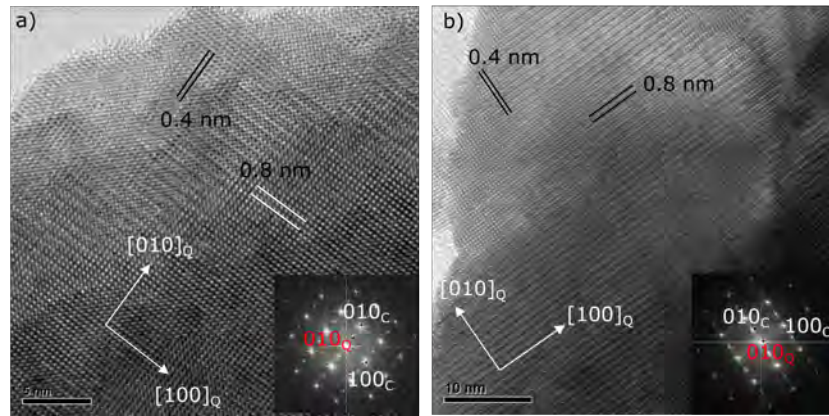


**Figure 4:** High resolution electron micrograph of a crystal of a) NNT and b) Er-NNT in the  $[001]_C$  zone axis. Insets show the corresponding Fast Fourier Transform, where Miller index in white and red correspond to the basic perovskite cell and to the Q phase, respectively.

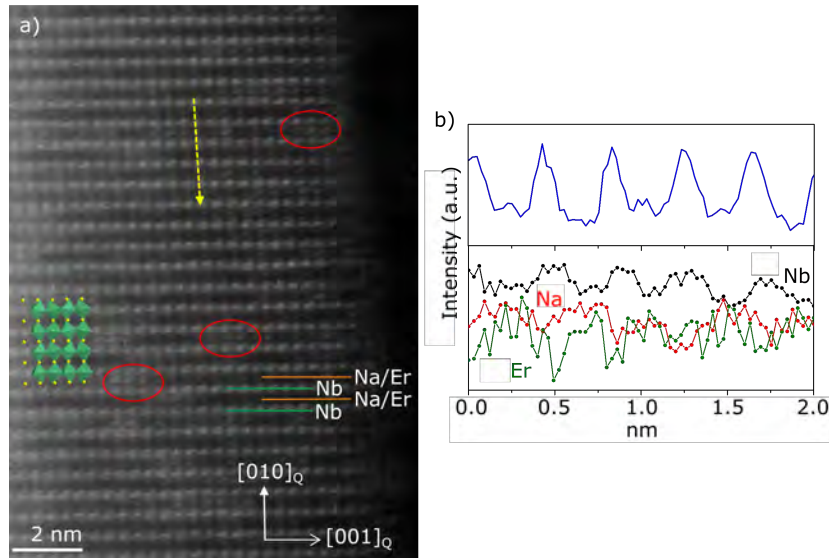


**Figure 5:** a) HAADF-STEM image of a crystal of Er-NNT in the  $[110]_C$  orientation ( $[100]_Q$ ). Er-enriched zones are circled in red on the image. The projected structure model has been overlapped as a help for the eye. b) The intensity profile from the image (yellow arrow in a) ) is shown above. The intensity maxima correspond to Nb positions along  $[010]$ . The EELS line-scans (from the line indicated by the yellow arrow in a) ) using  $\text{Nb-L}_{2,3}$ ,  $\text{Na-K}$  and  $\text{Er-M}_{4,5}$  signals are plotted below.

previously reported results on  $\text{Er}^{3+}$ -doped  $\text{NaNbO}_3$  have not shown information about the polar/non-polar nature of the synthesized phases and SHG emission is not studied [31]. However, authors referred to the prepared materials as outstanding UCF emitters, the emission intensity depending on erbium content which was closely related to  $\text{Er}^{3+}$  atomic site. Authors observed that optimal emission was obtained for 0.5 wt % and they reported that substitution took place at Nb sites for  $\text{Er}^{3+}$  content below 0.5 wt %, but further increasing content changed to sodium sites.

#### 4. Optical characterization

As shown in Figure 6 a), the spectra registered for the maximum compression point in the case of NNT show only SHG emission from 360 nm to 440 nm, as expected. However, Er-NNT (Figure 6 b) clearly shows both SH (in the same spectral range as NNT) and a typical UCF signal of the  $\text{Er}^{3+}$  ion, either using the pulses with and without the 980 nm band. Only the green UCF signal could be registered, since a UCF emission in the blue can be potentially hidden under the SH spectrum, while a UCF emission in the red is expected to be in a spectral region which overlaps with the laser spectrum, and hence it cannot be independently measured. The signal in the green is associated to the emission transitions taking place at 520 and 540 nm.

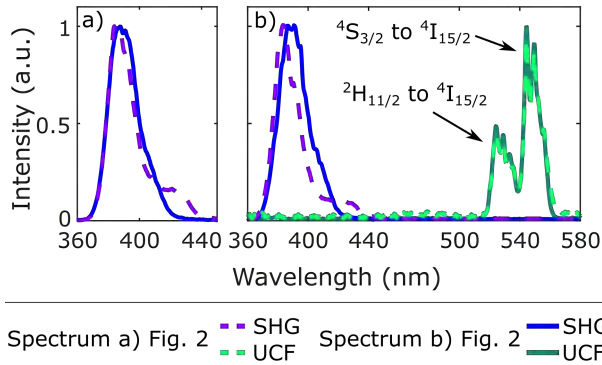


**Figure 6:** a) Normalized SHG spectra of NNT sample. b) Normalized SHG and UCF spectra of Er-NNT sample.

The width of the peaks, and therefore the intensity of the emission, depends on the crystal field effect and, more important in our case, on the concentration-quenching effect of  $\text{Er}^{3+}$  caused by energy transfer processes between neighbor  $\text{Er}^{3+}$  ions. This effect increases with dopant concentration and clustering of  $\text{Er}^{3+}$  ions. In this context, it is important to recall that HAADF-STEM images (Figure 5 a), clearly reveal Er-enriched areas on the crystal.

Subsequently, the SHG and UCF intensity emission responses of the samples with the laser intensity were checked. A set of neutral density filters was used to change the average power and hence the intensity at focus, where the sample was placed (Figure 1), and the wedges were then placed at the corresponding maximum-compression point. The laser input intensity was measured using a photodetector

(Thorlabs S121C), and SHG or UCF spectra were registered and integrated to obtain a value proportional to the intensity emitted by the sample. Figure 7 shows these integrated intensities versus the input intensity along with the fits to a  $I^x$  curve for NNT and Er-NNT samples. For SHG  $x_1=2.07$  was obtained for NNT, and  $x_2=1.99$  for Er-NNT, which are also good values when compared with the theoretical one  $x=2$ , that is, the measured quadratic dependency indicates the signal is generated from a second-order process. In addition,  $x_3=1.69$  is obtained for the green  $\text{Er}^{3+}$  UCF signal in Er-NNT, which is in agreement with results obtained by other authors [32–34]. In pure two-step one-photon processes,  $x=2$  value is expected. However, as previously mentioned, strong concentration-quenching effects highly impact both on the intensity of the emission as well as on the changes of energy-loss mechanisms which happen in the excited population dynamics via two- and three-photon processes. [35, 31, 36]. These effects can lead to different slopes in the logarithmic representation of intensity emission vs. input intensity, which depend on the different UC mechanisms involved in each case, mainly related to the way in which the intermediate levels are being populated or depopulated. It is worth noting that this behavior was also measured in

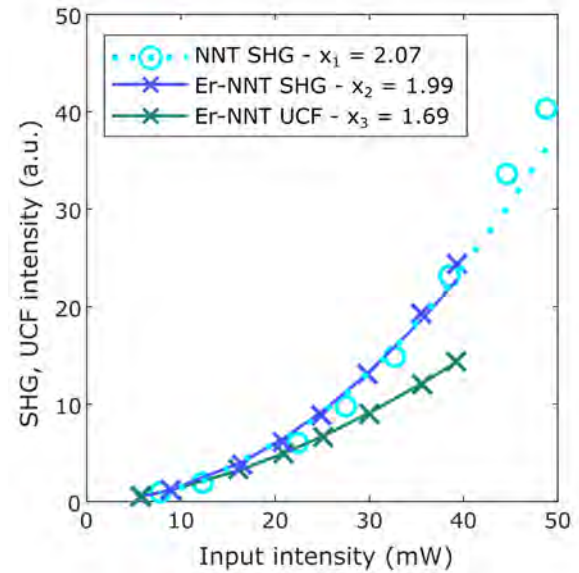


**Figure 7:** Intensity dependence  $I^x$  of the SHG generated in NNT ( $\circ$ ) and Er-NNT ( $\times$ ), and UCF in Er-NNT ( $\times$ ).

Er-NNT for other values of the glass insertion (not shown), i.e. for positively and negatively chirped pulses. For SHG,  $x$  values ranged between 1.9 to 2.0 were obtained in all cases, while for UCF  $x$  ranged from 1.7 to 1.8. These results indicate that for a given pulse (a pulse with a given chirp) a change in the total energy of the pulse leads to the respective  $I^x$  law for SHG and UCF signals regardless of the chirp of the pulses. In addition, since these sets of measurements took several hours and was taken irradiating the sample in the same spot, the fact that SHG and UCF signals kept their corresponding  $I^x$  responses is an evidence



of the photostability of these emissions. At this point, an interesting question would be to analyze the possibility of carrying out an effective control of the intensity of the SH and UC emissions of the Er-NNT particles, since this would be a very important step for further applications in in-vivo fluorescence microscopy.

To address this issue, we shape the laser pulse by modifying its coherent phase structure or "chirp" using the variable dispersion compressor consisting of DCM7 chirped mirrors and BK7 wedges. [25], which add an additional spectral phase  $\phi_g(\omega)$  to the pulse. Complete dispersion scans were performed for full laser energy (without the neutral density filters).

In Figure 8 the SHG signals generated in a NNT sample between 360 and 450 nm are displayed, normalized in intensity. Figure 8 a) and b) shows the SHG dispersion scan exciting with the pulse without the 980 nm band, while Figure 8 c) shows the SHG dispersion scan when exciting with the pulse with 980 nm band. Although both signals have

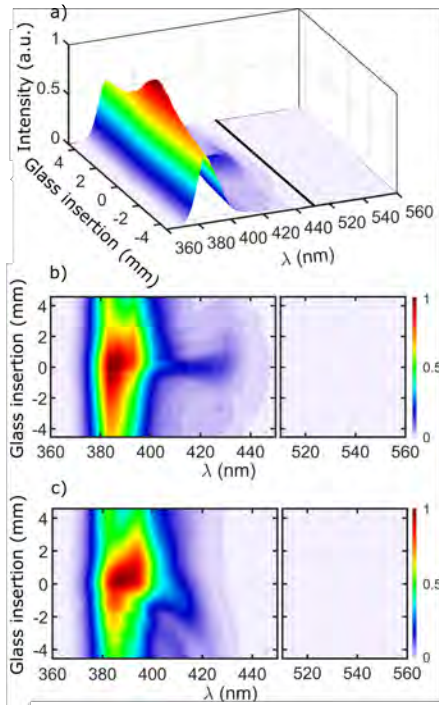


**Figure 8:** Normalized spectra of the SHG in NNT as a function of relative glass insertion: a) excitation without the 980 nm band in 3D display, b) idem in top view, c) excitation with the 980 nm band, in top view. Accumulation times: a) and b): 200 ms for SHG and 1000 ms for the UCF, c): 400 ms for SHG and 1000 ms in the UCF range.

spectral content between 360 and 450 nm, the differences in shape between b) and c) are evident since SHG is produced by pulses that differ both in spectrum and spectral phase. No emission appears around 510 nm and 560 nm, regardless the excitation spectrum used, but this zone is shown for later comparison with the UCF emitting samples.

When performing the same experiment with a sample of Er-NNT with and without the 980nm-band, in addition to a

SHG signal, green fluorescence spectra of  $\text{Er}^{3+}$  ions between 510 and 560 nm are also observed with distinct bands centered at 530 and 550 nm. Figure 9 shows these spectra as a function of the relative glass insertion (chirp). SHG and UCF signals in Figure 9 have been digitally superimposed taking care of representing them in the same intensity scale, since they were measured using different accumulation times. The UCF emission is clearly weaker than the SHG emission. Accumulation times for UCF were 5 times longer than for SHG to have an adequate measurement (200 ms for SHG and 1000 ms for UCF). As previously mentioned, the high erbium concentration is probably playing a role in the low UCF signal. As mentioned in the introduction,  $\text{Er}^{3+}$  has a small blue fluorescence band around 400 nm, which in our case is hidden by the strong SHG emission, while the red fluorescence band is hidden by the residual emission of the laser. Since the pulse is broadband, both the spectral zone of the pulses around 980 nm and 790 nm are contributing to the excitation of  $\text{Er}^{3+}$  ions in Figure 9 a2), but only 790 nm in Figure 9 b2). Notice that the SHG signals are similar to those obtained for NNT in Figure 8 and are chirp-sensitive.

In order to better ascertain the features of the  $\text{Er}^{3+}$  UCF, we represent in Figure 9 a3) and 9 b3) the same signals as in Figure 9 a2) and 9 b2) but normalized to its own maximum. It can be observed that in Er-NNT the SHG signals are still sensitive to the spectral phase of the pulse and the shapes are in fact very similar to the SHG signals of the non-doped NNT sample (Figure 8), while UCF shows a distinct depletion at the compression point (glass insertion 0). This behavior occurs for all wavelengths and the UCF spectrum is depleted as a whole at the compression point and is slightly asymmetric in intensity with the glass insertion. Similar behavior is observed when exciting with or without the 980 nm band. This is highlighted in Figure 10 where the SHG and UCF intensities (obtained by integrating their whole spectrum in  $\omega$ , respectively) are represented as a function of the glass insertion, being each one normalized to its maximum value. We observe that the SHG/UCF ratio changes and at the maximum compression point SHG reaches a maximum and UCF a minimum.

As the dependence of the SHG and the UCF on the excitation intensity follow the law  $I^2$  and  $I^{1.69}$ , respectively, an increase of signal is expected at  $\xi=0$  for both SHG and UCF emissions. However, UCF presents an asymmetric dip. The observation of preferential emission for negative chirp for Er-NNT implies that the observed enhancements are not only due to pulse width effects, but also to the magnitude and sign of the chirp, i.e. they depend on the order in which the different spectral components of the pulse arrive to the sample. To further strengthen our statements, Figure 11 a) and 11 b) display the variation of the integrated (in  $\omega$ ) UCF and SHG spectra of Er-NNT as a function of pulse chirp at various laser average powers (and hence, intensities). All experiments showed enhanced UCF with positively and negatively chirped pulses, compared to compressed pulses. For the less intense pulses, we find that there is less dependence of the UCF on the chirp. Increasing the intensity, the

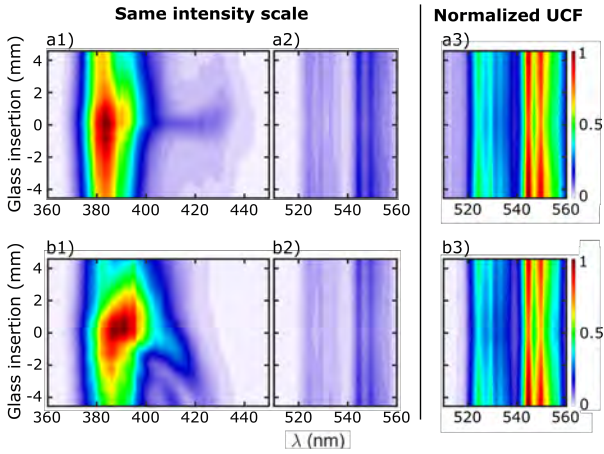


**Figure 9:** Spectra of the SHG and UCF in Er-NNT sample as a function of relative glass insertion excited by the pulse without the 980 nm band a) (a1), a2) and a3) or by the pulse without the 980 nm band b) (b1), b2) and b3). a1) SHG normalized to its own maximum. a2) UCF normalized to the maximum of a1). a3) UCF normalized to its own maximum, Idem for b1), b2) and b3). Accumulation times: a) 200 ms for SHG and 1000 ms for UCF, b) 200 ms for SHG and 400 ms for UCF.

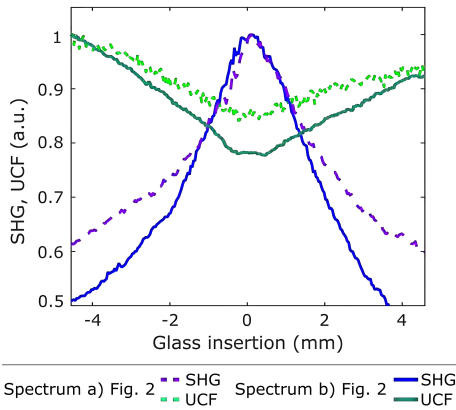


**Figure 10:** Normalized intensity of SHG and UCF at different relative glass insertions for excitation with and without the band at 980 nm.

asymmetry induced by the chirp is even more evident. On the contrary, the SHG signals show the same kind of behaviour for all the excitation intensities.

Such types of dependencies have been previously addressed in other molecular fluorescent systems via two-photon absorption [37, 38]. For example, the asymmetric response of fluorescence in the iodine molecule  $\text{I}_2$  to chirped femtosecond pulses was first reported by Shank and co-workers [39], and fluorescence depletion was observed for negatively chirped pulses and explained as an intrapulse pump-dump process that follows the nascent wave packet in the upper excited state as the carrier frequency shifts to lower energies. Different qualitative and quantitative interpretations of the chirp dependence of molecular fluorescence have been proposed to explain asymmetries in fluorescence. Cao

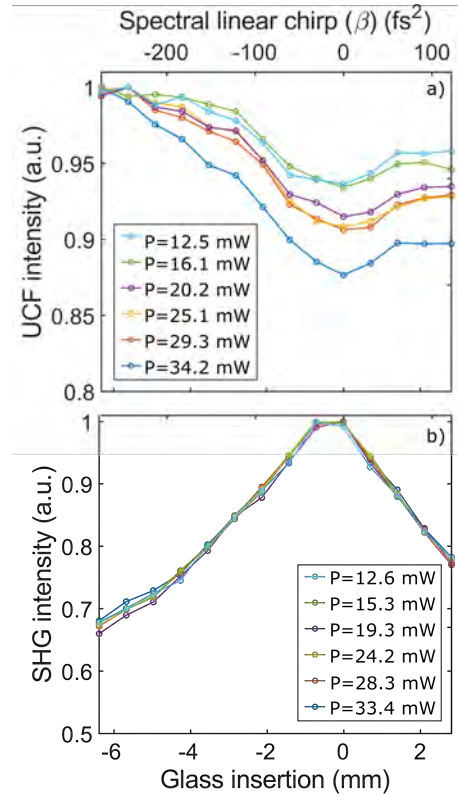


**Figure 11:** Normalized integrated signals as a function of relative glass insertions using different average laser powers. a) UCF, b) SHG.

et al. developed an intrapulse three level model [40]. The role of stimulated transitions without relaxation was discussed by Hashimoto et al. [41], while the competition between stimulated transition and relaxation has been discussed by Bardeen et al. [42] and Fainberg et al. [43].

In order to qualitatively explain the fluorescence results shown in Figure 11 a), we can accommodate the sequential resonance model, previously used by other authors,[44–46] to a stationary three-level model for the erbium ion shown in Figure 12 a). Unlike other models, which take into account the femtosecond vibrational wave-packet dynamics,[40, 47, 48] in the current case, the pulse duration is sufficiently short to assume that the nuclear configuration is approximately frozen during the impulsive excitation. Since in the laser spectrum the band around 766 nm is stronger than the one at 980 nm, and the fluorescence depletion shown in Figure 9 is observable with and without the contribution of the 980 nm band to the excitation of the  $\text{Er}^{3+}$  ion, we will concentrate on the most relevant transitions (Figure 12 a) that can take place exciting with a broadband laser with a central wavelength around 766 nm.[24] It can be seen that the observed green fluorescence may appear through two possible mechanisms. First, a sequential two-photon excitation process can be considered. In this process,  $\text{Er}^{3+}$  at the ground state is first pumped into a real intermediate level ( $^4\text{I}_{9/2}$ ) by absorption of one pump photon, then, simultaneously absorbs one pump photon again and it is promoted to the upper excited state



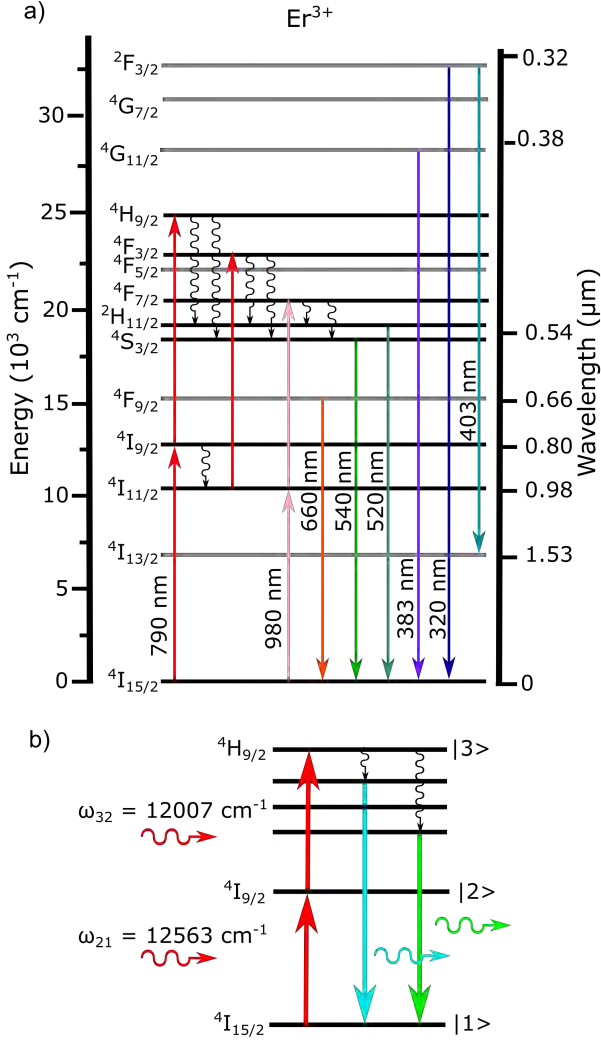


**Figure 12:** a) Basic energy levels in  $\text{Er}^{3+}$ . b) Sequential absorption and upconverted emission.

( $^4\text{H}_{9/2}$ ). When the interaction of the femtosecond laser pulse with  $\text{Er}$ -NNT is over,  $\text{Er}^{3+}$  will relax to the lower excited states  $^2\text{H}_{11/2}$  and  $^4\text{S}_{3/2}$  from which, the down-conversion occurs providing green fluorescence bands at 520 and 540 nm (see transitions in Figure 12 a). Secondly, an excited-state absorption process can be also present. In this case, the  $\text{Er}^{3+}$  at the ground state is first pumped to a real intermediate level ( $^4\text{I}_{9/2}$ ), the same as in the sequential two-photon excitation process, and then relaxes non-radiatively to the lower excited state  $^4\text{I}_{11/2}$ , from which the absorption of one pump photon again promotes the  $\text{Er}^{3+}$  ion to the upper excited state  $^4\text{F}_{3/2}$ . Finally, the ion relaxes to the lower excited states  $^2\text{H}_{11/2}$  or  $^4\text{S}_{3/2}$ , from which, the characteristic emission at 520 and 540 nm can take place again. However, this last process can be ignored since the femtosecond pulse duration is of the order of 10 fs while the lifetime of the level  $^4\text{I}_{9/2}$  is of the order of a few ns.[35, 49] Therefore, we propose a simplified model in which the fluorescence is produced via sequential two-photon resonant excitations, one from the

level  $^4\text{I}_{15/2}$  to the intermediate level  $^4\text{I}_{9/2}$  followed from a second excitation from this level to the excited level  $^4\text{H}_{9/2}$  and the subsequent fluorescence emission.

Let us denote the three atomic states shown in Figure 12 b) as  $|1\rangle$ ,  $|2\rangle$  and  $|3\rangle$ , with energies  $\hbar\omega_j$ . The transition frequencies associated to the wavenumber separations are  $\omega_{21}=12563 \text{ cm}^{-1}$  and  $\omega_{32}=12007 \text{ cm}^{-1}$ , respectively. The laser pulse is assumed to have a Gaussian temporal shape, with an electric field  $E(t)$  with frequency  $\omega_L$  ( $\lambda_L = 770 \text{ nm}$ ) given by:

$$E(t) = E_0 \sqrt{\frac{1}{(1 + i\beta\Gamma^2)}} \exp \left[ -\frac{t^2}{\tau_0^2} - i\omega_L t - i\beta t^2 \right] + c.c., \quad (1)$$

where  $E_0$ ,  $\tau_0$ ,  $b$ , and  $\Gamma$  are the amplitude, the temporal duration of the field (hence, the FWHM pulse duration is  $\sqrt{2 \ln 2} \tau_0$ ), the temporal linear chirp and the spectral bandwidth, respectively and  $\beta$  is the spectral linear chirp defined as:  $\beta = \frac{1}{2} \frac{\partial^2 \varphi_s(\omega, z)}{\partial \omega^2} \Big|_{\omega=\omega_0}$ .

The relations for these parameters are given as

$$\tau^2 = \frac{\tau_0^4 + \beta^2}{\tau_0^2} \quad b = \frac{\beta}{\tau_0^4 + \beta^2} \quad (2)$$

To calculate the time dependent molecular response, we used the density matrix formalism and solved the quantum Liouville equation [50]

$$\frac{d\rho}{dt} = -\frac{i}{\hbar} [H, \rho] - \gamma \rho, \quad (3)$$

where  $\rho$  is the density matrix which describes the system behaviour,  $\gamma$  is the attenuation coefficient of the density matrix component, and  $H$  is the Hamiltonian operator given by:

$$H = \hbar \sum_{j=1}^3 \omega_{jj} \sigma_{jj} - \hbar [\Omega_{21}(t) \sigma_{21} + \Omega_{32}(t) \sigma_{32} + H.c.], \quad (4)$$

where  $\sigma_{ij}$  are the Pauli operators,  $\Omega_{ij} = \mu_{ij} E(t)/\hbar$  are the Rabi frequencies of the optical transition and the parameters  $\mu_{ij}$  with  $(i, j=1,2,3)$  are the dipole matrix elements of the transitions, respectively.

The equations of motion for the density matrix elements in an appropriate rotating frame under the slowly-varying envelope (SVEA) and rotating-wave (RWA) approximations are:

$$\begin{aligned} \frac{\partial \rho_{31}}{\partial t} &= -i[\Delta_1 - 2bt]\rho_{31} + i\Omega_{21}(t)\rho_{21} \\ &\quad - i\Omega_{32}(t)\rho_{32}, \\ \frac{\partial \rho_{21}}{\partial t} &= -i[\Delta_1 + \Delta_2 - 4bt]\rho_{21} \end{aligned} \quad (5)$$

$$+ i\Omega_{21}(t)(\rho_{11} - \rho_{22}) + i\Omega_{32}(t)\rho_{31}, \quad (6)$$

$$\frac{\partial \rho_{32}}{\partial t} = -i[\Delta_2 - bt]\rho_{32} + i\Omega_{32}(t)(\rho_{22} - \rho_{33}) - i\Omega_{21}(t)\rho_{31}, \quad (7)$$

$$\frac{\partial \rho_{33}}{\partial t} = i\Omega_{32}(t)\rho_{23} - i\Omega_{23}(t)\rho_{32}, \quad (8)$$

$$\frac{\partial \rho_{22}}{\partial t} = i\Omega_{21}(t)\rho_{21} - i\Omega_{12}(t)\rho_{12}, \quad (9)$$

where  $\Omega_{21}(t) = \frac{\mu_{21}E(t)}{\hbar}$ ,  $\Omega_{32}(t) = \frac{\mu_{32}E(t)}{\hbar}$  are the Rabi frequencies,  $\Delta_1 = \omega_{21} - \omega_L$  and  $\Delta_2 = \omega_{32} - \omega_L$  the detunings associated to the transitions. In the Equation 5 to 9,  $\rho_{ij} = \rho_{ji}^*$  and  $\rho_{11} + \rho_{22} + \rho_{33} = 1$ . In the later equations, the relaxation processes were neglected since the timescale of the fluorescence relaxation rates ( $\mu\text{s}$ ) is much longer than the temporal duration of the field (fs).

In this context, population of the ground state of the system is given by the diagonal term of the density matrix  $\rho_{11}$ , while for the excited state it is obtained from  $\rho_{33}$ . The population dynamics has been obtained by numerical integration using a fourth-order Runge-Kutta algorithm of the density matrix equation by considering a pulse with a temporal duration of the field  $\tau_0 = 10$  fs choosing an approximate central wavelength of  $\lambda_L = 770$  nm as in the experiment. Thus, the detunings are  $\Delta_1 = -1.27 \times 10^4$  GHz and  $\Delta_2 = -9.7 \times 10^4$  GHz. The pulse energy is 0.6 nJ and the dipole coupling coefficients are assumed to be  $\mu_{21} = \mu_{32} = 1.85 \times 10^{-29}$  cm, which give Rabi frequencies  $\Omega_{21} = \Omega_{32} = 0.22\tau_0^{-1} \equiv \Omega$ . This corresponds to an intensity of the order of  $4.7 \times 10^9$  W/cm<sup>2</sup> at focus ( $I_{ij} = \frac{1}{2}c\epsilon_0 \left( \frac{\hbar\Omega_{ij}}{\mu_{ij}} \right)^2$ ). In our system we allow for a chirp parameter on the range of  $\beta = \pm 200$  fs<sup>2</sup>, as in the experiment, which corresponds to a range of glass insertion around  $\pm 5$  mm. In addition, we consider that initially the population is in the ground level, i.e.  $\rho_{11} = 1$ ,  $\rho_{22} = \rho_{33} = 0$  and all coherences are zero ( $\rho_{ij} = 0$ ).

In this theoretical model, the UCF emitted is proportional to the population of the excited level  $\rho_{33}$  ( $|3\rangle$ ) or  ${}^4\text{H}_{9/2}$ , so the influence of the spectral linear chirp  $\beta$  on the UCF properties can be easily examined. In Figure 13 a) the population  $\rho_{33}$  at the end of the excitation pulse is plotted as a function of the time for an excitation using positively chirped (PC,  $\beta=20$  fs<sup>2</sup>), negatively chirped (NC,  $\beta=-20$  fs<sup>2</sup>) and transform-limited pulses (TL,  $\beta=0$  fs<sup>2</sup>) with the initial condition of  $\rho_{11}=1$ . One can see that, after the pulse irradiation the remaining population in the uppermost level, i.e.  $\rho_{33}$ , is higher for the NC excitation than for the PC. For positive chirped and TL pulses, the leading part of the pulse populates level ( $|3\rangle$ ) and then the trailing edge of the pulse induces a depopulation. On the contrary, NC pulses produce a monotonous increase of the population until reaching a constant value. In all cases, the steady state is reached after 6 times the pulse duration approximately. Figure 13 b) displays the population of the state  $|3\rangle$  in the steady state as a function of the spectral linear chirp  $\beta$ . It can be seen that the final

population ( $\rho_{33}$ ) does not monotonously decrease with the increasing pulse duration caused by the chirp, which leads to an intensity decrease. Instead, we observe a behaviour which is much more sensitive to the sign of the chirp than to the pulse duration. Clearly, the population shows a deep depletion near  $\beta=0$  (which corresponds to a transform-limited pulse), and it is asymmetric left and right from this point. This behavior in the population is then transferred to the UCF, as experimentally measured (Figure 9). We see an enhancement of the  $\text{Er}^{3+}$  UCF in both directions of the chirp, but a bit more in the negative direction ( $\beta < 0$ ). It can also be seen that at low intensities, the influence of the chirp in the pulse is less relevant.

These data show how pulse coherence effects can become important at higher intensities where multiple photon transitions become more likely. Although this behaviour qualitatively agrees with the experimental results given in Figure 11 a), more studies are needed to analyze the role of  $\text{Er}^{3+}$  ion concentration and the influence of the other atomic levels involved. In any case, coherent control via linear chirping a femtosecond laser pulse holds the promise for a powerful tool in controlling the emission properties of the sample by properly selecting the laser wavelength, the repetition rate and the pulse duration, or temporally shaping the laser pulse.

## 5. Conclusions

$\text{NaNb}_{0.9}\text{Ti}_{0.1}\text{O}_{2.95}$  (NNT) and  $\text{Na}_{0.95}\text{Er}_{0.05}\text{Nb}_{0.9}\text{Ti}_{0.1}\text{O}_3$  (Er-NNT) polar perovskites have been successfully synthesized as nanostructured materials by microwave assisted hydrothermal method. NNT is an active SHG material which acts as an effective host for  $\text{Er}^{3+}$  ions. The microstructural characterization performed indicates that  $\text{Er}^{3+}$  is a bulk constituent of the crystals of Er-NNT by substituting for sodium in the A sublattice of the perovskite structure. With  $\text{Er}^{3+}$  ions as luminescent emitters, Er-NNT behaves as a bifunctional material by simultaneously generating SHG and UCF signals when pumped by a broadband Titanium:Sapphire laser oscillator with a few fs pulse duration. Dependence of SHG and UCF emissions on the excitation intensity ( $I^x$  law) of the laser has been studied. A pure quadratic ( $x=2$ ) behaviour has been found in SHG as expected, while UCF showed a lower intensity dependence ( $x=1.69$ ), which is compatible with having interactions among closely placed  $\text{Er}^{3+}$  ions.

Sensitivity of both SHG and UCF emissions to the chirp of the exciting pulses has been demonstrated by using two different excitation spectra, both with a band at 766 nm and eventually with a second band at 980 nm,  $\text{Er}^{3+}$  ions being excited by any of them. Moreover, UCF signal is weaker for compressed pulses and asymmetric with the sign of the chirp. A model based on the density matrix equations has been proposed to reproduce the general features of the UCF with the chirp of the pulses. This means that, to some extent, quantum interference effects are present in Er-NNT. From the obtained results, the 980 nm band does not seem to play a major role in the optical behaviour of these oxides, probably

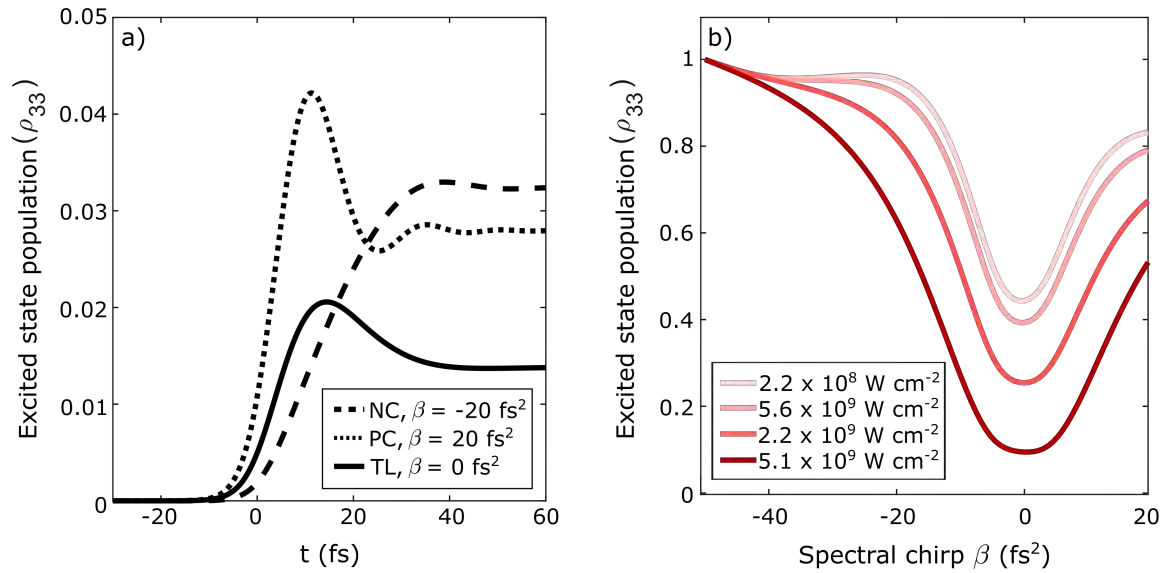


**Figure 13:** a) Populations of level  $|3\rangle$  ( $\rho_{33}$ ) are plotted as a function of time for  $\beta=20 \text{ fs}^2$  (PC),  $\beta=-20 \text{ fs}^2$  (NC) and  $\beta=0 \text{ fs}^2$  (TL). b) Dependence of the steady state population  $\rho_{33}$  on the spectral linear chirp  $\beta$  at different pulse intensities.

due to its lower intensity in respect to the 766 nm band. Similar experiments could then be performed using non octave-spanning commercial oscillators without emission at the 980 nm band. The fact that both SHG and UCF signals are sensitive to the spectral phase of the exciting pulses suggests the use of Er-NNT for coherent control. The well-established importance of the sodium niobate (NN) perovskite material in a wide range of applications, is thus reinforced by the dual behaviour that we report in this work. It opens the way to the development of biocompatible erbium-doped non-centrosymmetric perovskites with optimal dual light emission for optical microscopy and bioimaging.

## Acknowledgements

E. García-González and S. García-Martín thank MICINN/AEI for funding the project PID2019-106662RB-C44/AEI/10.13039/501100011033 and R. Weigand thanks MINECO/AEI for funding the project FIS2017-87360-P. O. Pérez-Benito acknowledges a predoctoral contract from UCM (call CT63/19-CT64/19).

We acknowledge the help of O. Contreras in the development of the synthesis experiments.

We will always be indebted to Professor E. Morán for the knowledge transmitted, he left us too early, untimely.

## CRedit authorship contribution statement

**Óscar Pérez-Benito:** Software, Investigation, Writing - Original Draft. **Miguel Ángel Antón:** Conceptualization, Methodology, Software, Writing - Original Draft. **Esteban Urones-Garrote:** Investigation. **Susana García-Martín:** Conceptualization, Investigation, Writing - Original Draft,

Funding acquisition. **Ester García-González:** Conceptualization, Investigation, Writing - Original Draft, Funding acquisition. **Rosa Weigand:** Conceptualization, Methodology, Investigation, Writing - Original Draft, Funding acquisition.

## References

- [1] D. Jaque, C. Richard, B. Viana, K. Soga, X. Liu, J. G. Solé, Inorganic nanoparticles for optical bioimaging, *Advances in Optics and Photonics* 8 (2016) 1–103.
- [2] A. Polman, H. A. Atwater, Plasmonics: optics at the nanoscale, *Materials Today* 8 (2005) 56.
- [3] Y. Liu, D. Tu, H. Zhu, X. Chen, Lanthanide-doped luminescent nanoprobes: controlled synthesis, optical spectroscopy, and bioapplications, *Chemical Society Reviews* 42 (2013) 6924–6958.
- [4] G. Chen, H. Qiu, P. N. Prasad, X. Chen, Upconversion nanoparticles: design, nanochemistry, and applications in theranostics, *Chemical Reviews* 114 (2014) 5161–5214.
- [5] L. Bonacina, P.-F. Brevet, M. Finazzi, M. Celebrano, Harmonic generation at the nanoscale, *Journal of Applied Physics* 127 (2020) 230901.
- [6] C. Vonesch, F. Aguet, J.-L. Vonesch, M. Unser, The colored revolution of bioimaging, *IEEE Signal Processing Magazine* 23 (2006) 20–31.
- [7] B. E. Cohen, Beyond fluorescence, *Nature* 467 (2010) 407–408.
- [8] P. Pantazis, J. Maloney, D. Wu, S. E. Fraser, Second harmonic generating (shg) nanoprobes for in vivo imaging, *Proceedings of the National Academy of Sciences* 107 (2010) 14535–14540.
- [9] X. Liu, C.-H. Yan, J. A. Capobianco, Photon upconversion nanomaterials, *Chemical Society Reviews* 44 (2015) 1299–1301.
- [10] F. Wang, X. Liu, Recent advances in the chemistry of lanthanide-doped upconversion nanocrystals, *Chemical Society Reviews* 38 (2009) 976–989.
- [11] D. Jaque, L. M. Maestro, B. Del Rosal, P. Haro-Gonzalez, A. Benayas, J. Plaza, E. M. Rodríguez, J. G. Solé, Nanoparticles for photothermal therapies, *Nanoscale* 6 (2014) 9494–9530.
- [12] D. N. Nikogosyan, *Nonlinear optical crystals: a complete survey*, Springer Science & Business Media, 2006.
- [13] L. Mayer, G. Dantelle, V. Jacques, S. Perruchas, G. Patriarche, J.-F. Roch, T. Gacoin, Dual light-emitting nanoparticles: second harmonic



- generation combined with rare-earth photoluminescence, *Journal of Materials Chemistry C* 2 (2014) 7681–7686.
- [14] S. Regny, J. Riporto, Y. Mugnier, R. Le Dantec, S. Kodjikian, S. Pairis, I. Gautier-Luneau, G. Dantelle, Microwave synthesis and up-conversion properties of SHG-active  $\alpha$ -(La, Er)( $\text{IO}_3$ )<sub>3</sub> nanocrystals, *Inorganic Chemistry* 58 (2019) 1647–1656.
  - [15] F. A. Rabuffetti, S. P. Culver, J. S. Lee, R. L. Brutchey, Local structural investigation of  $\text{Eu}^{3+}$ -doped  $\text{BaTiO}_3$  nanocrystals, *Nanoscale* 6 (2014) 2909–2914.
  - [16] D. Meshulach, Y. Silberberg, Coherent quantum control of two-photon transitions by a femtosecond laser pulse, *Nature* 396 (1998) 239–242.
  - [17] N. Dudovich, B. Dayan, S. M. G. Faeder, Y. Silberberg, Transform-limited pulses are not optimal for resonant multiphoton transitions, *Physical Review Letters* 86 (2001) 47.
  - [18] Z. Amitay, A. Gandman, L. Chuntanov, L. Rybak, Multichannel selective femtosecond coherent control based on symmetry properties, *Physical Review Letters* 100 (2008) 193002.
  - [19] R. Bartels, S. Backus, E. Zeek, L. Misoguti, G. Vdovin, I. Christov, M. Murnane, H. Kapteyn, Shaped-pulse optimization of coherent emission of high-harmonic soft X-rays, *Nature* 406 (2000) 164–166.
  - [20] G. Kim, J. Yang, B. Lee, S. Chizhov, A. Kalintsev, V. Yashin, U. Kang, et al., Efficient generation of the second and third harmonics of high-power femtosecond  $\text{Yb:KGW}$ -laser radiation in nonlinear-optical BBO crystals, *Journal of Optical Technology* 83 (2016) 463–467.
  - [21] X. Shang, P. Chen, W. Cheng, K. Zhou, J. Ma, D. Feng, S. Zhang, Z. Sun, J. Qiu, T. Jia, Fine tunable red-green upconversion luminescence from glass ceramic containing 5%  $\text{Er}^{3+}:\text{NaYF}_4$  nanocrystals under excitation of two near infrared femtosecond lasers, *Journal of Applied Physics* 116 (2014) 063101.
  - [22] G. Gouget, M. Duttine, U.-C. Chung, S. Fourcade, F. Mauvy, M.-D. Braidat, T. Le Mercier, A. Demourgues, High ionic conductivity in oxygen-deficient Ti-substituted sodium niobates and the key role of structural features, *Chemistry of Materials* 31 (2019) 2828–2841.
  - [23] R. Weigand, M. Miranda, H. Crespo, Oscilador láser de titanio: zafiro de 2 ciclos ópticos, Titanium: sapphire laser oscillator delivering two-optical-cycle pulses., *Optica Pura y Aplicada* 46 (2013) 105.
  - [24] L. Zhang, H. Hu, The fluorescence properties of highly-doped erbium fluoroaluminate glass pumped at 800 and 980 nm, *Journal of Non-crystalline Solids* 326 (2003) 353–358.
  - [25] Ó. Pérez-Benito, R. Weigand, Nano-dispersion-scan: measurement of sub-7-fs laser pulses using second-harmonic nanoparticles, *Optics Letters* 44 (2019) 4921–4924.
  - [26] J. Rödel, K. G. Webber, R. Dittmer, W. Jo, M. Kimura, D. Damjanovic, Transferring lead-free piezoelectric ceramics into application, *Journal of the European Ceramic Society* 35 (2015) 1659–1681.
  - [27] K. B. Chang, B. W. Edwards, L. Frazer, E. J. Lenferink, T. K. Stanev, N. P. Stern, J. C. Nino, K. R. Poeppelmeier, Hydrothermal crystal growth, piezoelectricity, and triboluminescence of  $\text{KNaNbOF}_5$ , *Journal of Solid State Chemistry* 236 (2016) 78–82.
  - [28] A. Sakowski-Cowley, K. Łukaszewicz, H. D. Megaw, The structure of sodium niobate at room temperature, and the problem of reliability in pseudosymmetric structures, *Acta Crystallographica Section B: Structural Crystallography and Crystal Chemistry* 25 (1969) 851–865.
  - [29] V. Shuvaeva, M. Y. Antipin, R. Lindeman, O. Fesenko, V. Smotrakov, Y. T. Struchkov, Crystal structure of the electric-field-induced ferroelectric phase of  $\text{NaNbO}_3$ , *Ferroelectrics* 141 (1993) 307–311.
  - [30] M. Ahtee, A. Glazer, H. Megaw, The structures of sodium niobate between 480 and 575 °C, and their relevance to soft-phonon modes, *Philosophical Magazine* 26 (1972) 995–1014.
  - [31] Y.-Y. Ge, Y.-J. Zhao, X.-Y. Yuan, S.-Y. Sun, Y.-Z. Zhao, H.-P. Zhou, Synthesis of  $\text{Er}^{3+}$ -doped perovskite nanorods with outstanding UC PL behavior, *RSC Advances* 6 (2016) 67353–67360.
  - [32] J. Suyver, A. Aebischer, S. García-Revilla, P. Gerner, H. Güdel, Anomalous power dependence of sensitized upconversion luminescence, *Physical Review B* 71 (2005) 125123.
  - [33] C. Joshi, K. Kumar, S. Rai, Upconversion and anomalous power dependence in  $\text{Ca}_{12}\text{Al}_{14}\text{O}_{33}:\text{Er}^{3+}/\text{Yb}^{3+}$  single phase nanophosphor, *Journal of Applied Physics* 105 (2009) 123103.
  - [34] J. Liao, Z. Yang, J. Sun, S. Lai, B. Shao, J. Li, J. Qiu, Z. Song, Y. Yang, Preparation and upconversion emission modification of crystalline colloidal arrays and rare earth fluoride microcrystal composites, *Scientific Reports* 5 (2015) 1–8.
  - [35] F. Auzel, Upconversion and anti-stokes processes with f and d ions in solids, *Chemical Reviews* 104 (2004) 139–174.
  - [36] J. Zhao, Z. Lu, Y. Yin, C. McRae, J. A. Piper, J. M. Dawes, D. Jin, E. M. Goldys, Upconversion luminescence with tunable lifetime in  $\text{NaYF}_4:\text{Yb}$ ,  $\text{Er}$  nanocrystals: role of nanocrystal size, *Nanoscale* 5 (2013) 944–952.
  - [37] A. Nag, D. Goswami, Effect of linear chirp on femtosecond two-photon processes in solution, *Journal of Spectroscopy and Dynamics* 2 (2012).
  - [38] A. Konar, V. V. Lozovoy, M. Dantus, Solvent environment revealed by positively chirped pulses, *The Journal of Physical Chemistry Letters* 5 (2014) 924–928.
  - [39] G. Cerullo, C. J. Bardeen, Q. Wang, C. V. Shank, High-power femtosecond chirped pulse excitation of molecules in solution, *Chemical Physics Letters* 262 (1996) 362–368.
  - [40] J. Cao, J. Che, K. R. Wilson, Intrapulse dynamical effects in multiphoton processes: Theoretical analysis, *The Journal of Physical Chemistry A* 102 (1998) 4284–4290.
  - [41] N. T. Hashimoto, K. Misawa, R. Lang, Three-level picture for chirp-dependent fluorescence yields under femtosecond optical pulse irradiation, *Applied Physics Letters* 82 (2003) 2749–2751.
  - [42] C. J. Bardeen, J. Cao, F. L. Brown, K. R. Wilson, Using time-dependent rate equations to describe chirped pulse excitation in condensed phases, *Chemical Physics Letters* 302 (1999) 405–410.
  - [43] B. Fainberg, V. Gorbunov, Coherent population transfer in molecules coupled with a dissipative environment by an intense ultrashort chirped pulse, *The Journal of Chemical Physics* 117 (2002) 7222–7232.
  - [44] S. Zhang, S. Xu, J. Ding, C. Lu, T. Jia, J. Qiu, Z. Sun, Single and two-photon fluorescence control of  $\text{Er}^{3+}$  ions by phase-shaped femtosecond laser pulse, *Applied Physics Letters* 104 (2014) 014101.
  - [45] C. Serrat, J. Biegert, Energy efficient method for two-photon population transfer with near-resonant chirped pulses, *Optics Express* 16 (2008) 19667–19673.
  - [46] A. Konar, V. V. Lozovoy, M. Dantus, Solvation stokes-shift dynamics studied by chirped femtosecond laser pulses, *The Journal of Physical Chemistry Letters* 3 (2012) 2458–2464.
  - [47] K. Misawa, T. Kobayashi, Wave-packet dynamics in a cyanine dye molecule excited with femtosecond chirped pulses, *The Journal of Chemical Physics* 113 (2000) 7546–7553.
  - [48] E. Heesel, B. Garraway, J. Marangos, Analysis of adiabatic passage by light-induced potentials with chirped laser pulses in three- and four-level diatomic systems, *The Journal of Chemical Physics* 124 (2006) 024320.
  - [49] R. Scheps, Upconversion laser processes, *Progress in Quantum Electronics* 20 (1996) 271–358.
  - [50] M. Joffre, Coherent effects in femtosecond spectroscopy: a simple picture using the Bloch equation, in: *Femtosecond Laser Pulses*, Springer, 2005, pp. 283–308.

## Appendix A: X-ray diffraction patterns

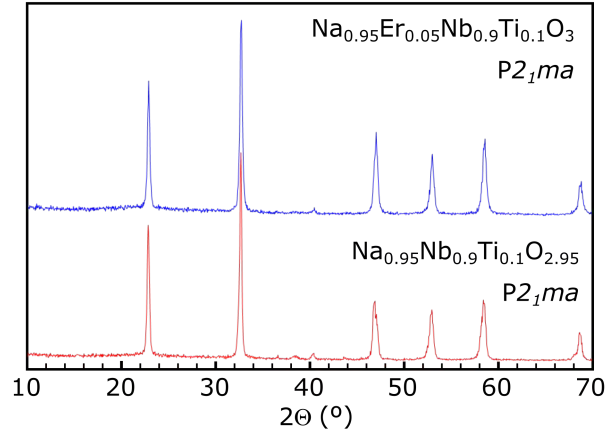


**Figure A1:** Powder X-ray diffraction patterns of NNT and Er-NNT samples. Patterns were unambiguously assigned to the non-centrosymmetric  $P2_1ma$  space group after a detailed characterization by transmission electron microscopy (see text.)